SCIENCE CHINA
Technological Sciences

•Article•

August 2021 Vol.64 No.8: 1663–1675
https://doi.org/10.1007/s11431-020-1766-y

Adjustable stiffness elastic composite soft actuator for fast-moving robots

GUO XinYu, LI WenBo & ZHANG WenMing*

State Key Laboratory of Mechanical System and Vibration, School of Mechanical Engineering, Shanghai Jiao Tong University, Shanghai 200240, China

Received August 14, 2020; accepted December 28, 2020; published online June 17, 2021

The application of soft pneumatic actuators is typically hindered by the low strength and slow response speed caused by their intrinsic material limitation and unstressed stable form. In this work, we present a design strategy for improving the performance and response speed for Pneu-Nets actuators by incorporating adjustable elastic components to form the elastic composite pneumatic actuator (ECPA). The elastic energy storage of the elastic component is implemented to enhance the capability and speed up the response of ECPA and pre-bend the actuator. Due to the design principle, the fully-flexible ECPA is easy to manufacture and regulate. Theoretical modeling and experiments are implemented to reveal the fast response characteristics and adjustable mechanical characteristics of ECPA. Experimental results show that the deflation response speed of ECPA is increased by at least 3.1 times with the action of elastic components, what is more, the stiffness of ECPA is increased by 22 times. Based on the ECPA, two kinds of locomotion robots including a running robot (runs at an average locomotion speed of 6.3 BL/s (body lengths, BL)) and an underwater swimming robot (achieves an average speed of 1.1 BL/s) are designed. The fast-moving robots both demonstrate high-speed mobility because of the rapid response and high strength of ECPA.

pneumatic actuator, fast response, adjustable stiffness, pre-bending actuator, fast-moving robots

Citation: Guo X Y, Li W B, Zhang W M. Adjustable stiffness elastic composite soft actuator for fast-moving robots. Sci China Tech Sci, 2021, 64: 1663–1675, https://doi.org/10.1007/s11431-020-1766-y

1 Introduction

Flexible pneumatic actuators have recently attracted increasing research interest in the modern time [1]. These malleable components interact with the environment like living organisms because of their flexibility, adaptability and security [2]. However, the intrinsic material properties and unstressed stable form of the pneumatic actuator limit the performance, resulting in slow response speed and low mechanical properties [3]. Therefore, how to compensate for the defects caused by the material and structure of pneumatic actuator has attracted tremendous research interest.

In order to improve the capabilities of flexible actuators, various accessories are used to assist the execution of actuators [4,5]. The accessories mainly include: smart materials modules [6–8], variable stiffness mechanisms [9,10], and blocking structures [11,12], etc. The smart materials such as low melting point alloys greatly increase the strength of the flexible actuator while retaining the flexibility and compliance of the flexible actuator [13]. However, the response speed of smart materials is slow, especially the process of cooling the smart material takes a lot of time. Variable stiffness mechanisms such as ratchet and pawl mechanism increase the stiffness of the actuator, but the mechanical structure is relatively large and greatly increases the weight and the response time of flexible actuator [14]. In addition, negative pressure is used in the blocking structure to increase the rigidity of the soft actuator. The speed of adjustment of blocking structure is fast, but the blocking may occur, and the effect of the stiffness is not obvious [15]. The addition of the

*Corresponding author (email: wenmingz@sjtu.edu.cn)

accessories improves the mechanical performance of the pneumatic actuator, but has no positive significance for improving the response speed.

The slow response speed limits the driving frequency and therefore degrades performance of soft actuator. To improve the performance and the response speed of the soft actuator, an initially curved structure for the rapid and programmable actuation of soft actuators exploiting elastic energy storage is a simple strategy [16]. Scarfogliero et al. [17] designed a miniature jumping robot by using an elastic energy storage and a release mechanism. Then, the elastic elements are used to store elastic energy and keep the initial bending angle of the actuator, which strongly reduces the relative mean power (W/kg) needed by the motor to actuate the gait [18,19]. Duduta et al. [20] proposed a high-speed soft robot based on dielectric elastomer actuators. The crawling robot achieves high-speed motion (1 BL/s) with a small size (20 mm long × 10 mm wide). In addition, the pre-bending strategy is also applicable to pneumatic actuators. A tethered pneumatic-actuated winding-styled soft rod-climbing robot that consists of two pre-bending actuators and a telescopic actuator is proposed, achieving speed of 30.85 mm/s (0.193 body length/s), and carrying a larger payload (weight 500 g, more than 25 times its self-weight) [21].

Implementing pre-bending actuators by storing elastic energy greatly improves the response speed and performance of soft actuators [22,23]. Inspired by this strategy, the Pneu-Nets actuator has also been improved. Li et al. [24] proposed a new approach to soft robot design based on pre-charged pneumatics, the soft bending actuator is actuated by pre-charged air pressure and retracted by inextensible tendons. The air pressure in the pre-charged soft actuator can be modulated by pulling or releasing the tendons, and hence adjusting its bending angle without additional energy consumption. What is more, the soft bending actuator controlled by tendons has a more precise action. Then, Wang et al. [25] proposed a prestressed soft actuator, the chamber part of the actuator is stretched longitudinally and sealed by gluing the cover onto the layer. The prestressed actuator has an initial curved statue due to the remaining prestress when the actuator is released, achieving a large deformation. What is more, Pal et al. [26] reported a three-finger pre-stressed soft actuator by joining a flexible strain limiting material (paper) to a pre-stressed elastomeric layer containing a pneumatic channel. This actuator achieves recovery times as low as 50 ms thanks to the release of the elastic energy stored in the actuator during actuation, significantly improving the actuation rates of pneumatic soft actuators after motions requiring large deformations. However, the prestressed actuator has a complicated production process and small stiffness. To further improve the performance of the pneumatic actuator, a spine-inspired fast and strong soft machines is proposed [27]. This design leverages tunable snap-through biostability to achieve the rapidly store and release energy within tens of milliseconds of soft actuator. Based on this actuator, the cheetah-like galloping crawler (2.68 body length/s) and high-speed underwater swimmer (0.78 body length/s) are developed. However, for flexible actuators, the addition of rigid materials may weaken the compliance and safety of flexible components.

This research proposes a new design strategy by combining Pneu-Nets actuator and elastic element to constitute the ECPA. The pre-tightened elastic element exerts the pre-loading force on the Pneu-Nets actuator, which improves the response speed and mechanical performance of the actuator while retaining the characteristics of fully-flexibility. By adjusting the pre-loading force of the elastic element, the elastic energy stored in the ECPA is changed accordingly, and the performance of ECPA can be adjusted. The pre-charged pneumatic soft actuators described in ref. [24] do not require complicated pneumatic control systems and can be precisely controlled. However, the ECPA is more mobile and flexible than the precharged pneumatic soft actuators, and ECPA can achieve faster response speed due to the elastic potential energy stored in the elastic pretension ropes. Due to the fast response and high-strength characteristics of ECPA, the bionic quadruped robot and the bionic manta ray swimming robot are designed and show fast-moving performance. The rest of this article is described as follows. The structural design and working principle are presented in Sect. 2. Sect. 3 provides detailed information about the modeling. The experiments and results of the output force, response speed and morphological characteristics are provided in Sect. 4. The performance of the bionic quadruped running robot and bionic manta ray swimming robot are demonstrated in Sect. 5. The relevant conclusion of this study is presented in Sect. 6.

2 Design and working principle

Figure 1(a) shows the conceptual structure and physical mechanism of ECPA. It consists of only two components: a Pneu-Nets bending actuator and an elastic element (rubber elastic cord with a diameter of 2 mm). The elastic cord is pre-tensioned to store the elastic potential energy to regulate the response speed and the mechanical characteristics of ECPA. Moreover, the geometric characteristics such as the pre-bending state of ECPA can also be adjusted by elastic elements. The components that make up the ECPA are all flexible parts, thus this simple design maintains the flexibility of the pneumatic actuator. Figure 1(b) shows the cross-sectional view of ECPA. The working principle of the ECPA is shown in Figure 1(c). In the initial state, the air chambers of the actuator are pressed together under the tension of the elastic cord, which causes the initial bending

state of the actuator. When the compressed air is input to the ECPA, the air chambers expand and squeeze each other, the air pressure in the air chambers resists the pretension of the elastic cord, resulting in a stretch and wide range of the bending angle change of ECPA. What is more, the pre-loading force greatly improves the deflation response speed of ECPA. The comparison of deflation response speeds of ECPA under the pre-loading force of 0 and 3 N is shown in Figure 1(d). When the air pressure of the pneumatic actuator falls from 60 to 0 kPa, the ECPA under the pre-loading force of 0 N takes 0.45 s to return to the initial state, the angular velocity of the bending angle is 6.2 rad/s. But the ECPA under the pre-loading force of 3 N takes only 0.24 s, achieving the angular velocity of the bending angle of 16.1 rad/s.

Figure 2 illustrates the fabrication process of the Pneu-Nets bending actuator which is mainly made of silicone. The Pneu-Nets actuator mainly consists of two parts: the main body, and a base which contains the inextensible paper layer. As shown in Figure 2(a) and (b), the main body is cast in upper and lower mold, two rods are installed on both sides of the upper mold to form a through hole of the Pneu-Nets actuator for fixing the elastic cord. To make this Pneu-Nets bending actuator, the main body and the base are cast separately and then stuck together, as shown in Figure 2(c).

The pre-tension of the elastic cord is applied through the force meter, as shown in Figure 3(a). In this way, the pre-loading force applied to the actuator can be accurately adjusted. Then, the end of the elastic cord is fastened to the bracket by the blockage (screw) to maintain the pre-loading force, as shown in Figure 3(b). To characterize the mechanical property of the elastic cord, a uniaxial tensile test is set. The experimental setting and results are shown in Figure 3(c). The initial length of the tested elastic rope is 19 mm, which is equivalent to the length of the elastic rope in ECPA. The end of the elastic cord is fixed on the bracket, and the other end is fixed on the force sensor (DYLY-105, China, scale 2 kg, accuracy 0.03%). The force sensor is installed in a slide table which is driven by a motor through the screw nut mechanism to perform the motion at a constant speed (1 mm/s). When the elastic rope is stretched, the force sensor collects the value of the tension. The test is repeated three times, and the average value is used to draw the stiffness curve. As shown in Figure 3(c), to simplify analysis and calculation, the stiffness curve is approximated as linear,

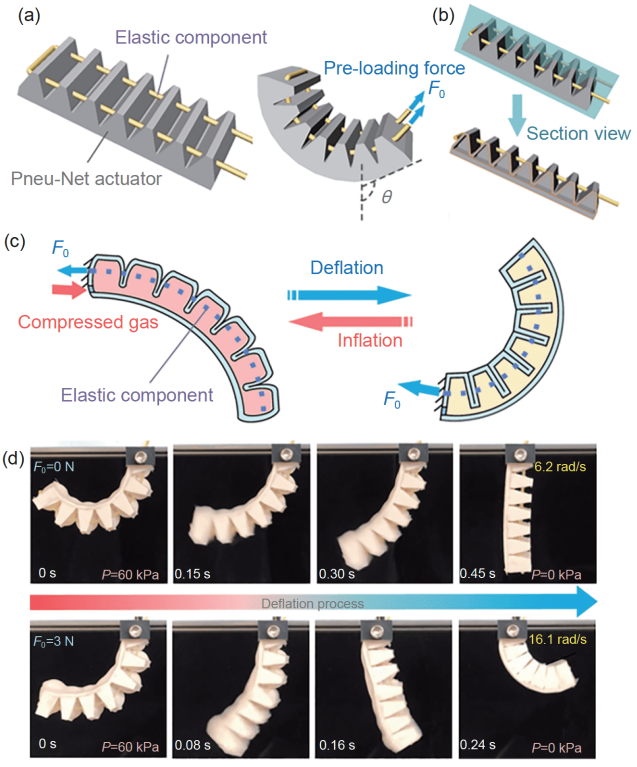

Figure 1 (Color online) Design and principle of ECPA. (a) Conceptual structure design of ECPA; (b) the cross profile of ECPA; (c) working principle; (d) comparison of the deflation response speed of ECPA under different pre-loading forces.

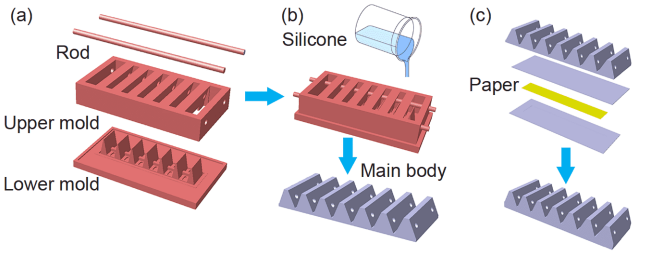

Figure 2 (Color online) Fabrication process of ECPA. (a) Exploded view of the mold; (b) the casting process of main body; (c) the components of the pneumatic actuator.

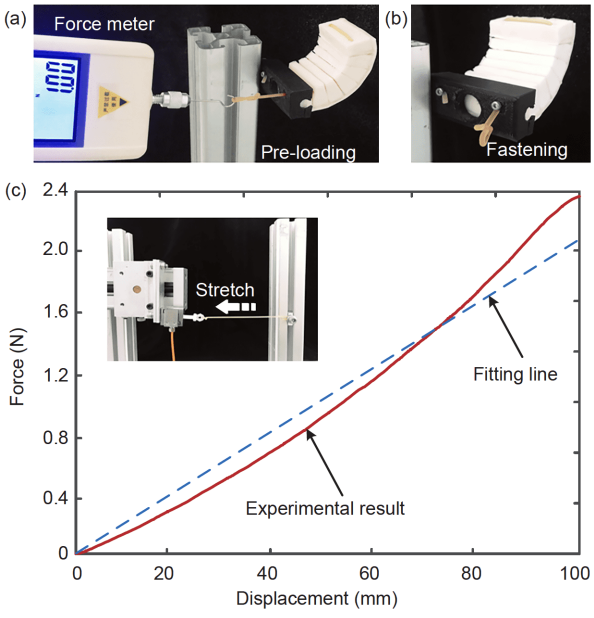

Figure 3 (Color online) The pre-tension and characterization of elastic cord. (a) Preload the elastic cord; (b) fasten the elastic cord way to maintain the pre-loading force of elastic cord; (c) the test and characterization on mechanical property of the elastic cord.

therefore, linear fitting is conducted for the result by the least square method, the slope of the fitting line is the elastic cord's stiffness value k_c (k_c=0.02 N/mm).

3 Modeling

To quantify the properties of ECPA, theoretical modeling is performed in this section. Based on the conventional fast response Pneu-Nets bending actuator and the performance requirements of ECPA, the geometry of the ECPA is designed and the hyperelastic silicone material is selected to cast the Pneu-Nets bending actuator. Then, according to the results of the pre-tests of ECPA, the dimensions of ECPA are optimized to improve its performance. The design and material parameters of the ECPA are shown in Table 1. Some assumptions are made to simplify the model and neglect the minor factors: (1) the actuator has no radial deformation; (2) the volume of the silicone material is assumed to be constant; (3) the length of the base layer of the Pneu-Nets actuator is assumed to be constant [28]. Based on the above assumptions, the bending of ECPA is mainly contributed by the expansion of the lateral wall of air chamber. Because all the lateral wall has the same geometrical properties, the deformation of a single lateral wall is calculated to analysis the deformation of the ECPA. The lateral wall is simplified as a deformable elastic rectangular membrane (a×b×h) with four edges fixed. Due to the hyperelastic nature of the selected silicone, a second order hyperelastic mathematical model, Yeoh model, is used to fully describe the compression and extension phases of the material with coefficients C_1=0.11 and C_2=0.02. What is more, empirically, second order Yeoh model provides a good fit to the properties of the selected silicone [29,30]. According to the second order Yeoh's theory, the total strain energy E can be given by

$$E=\int_{-h/2}^{h/2}\int_{-a/2}^{a/2}\int_{-b/2}^{b/2}C_1(I_1-3)+C_2(I_1-3)^2\mathrm{d}x\mathrm{d}y\mathrm{d}z, \tag{1}$$

where C_1, C_2 are the material parameters for silicone, I_1, I_2 represent the deformation tensor invariant. The total strain energy E can be expressed as

Table 1 Design and material parameters of the ECPA

Parameters	Values
Length of rectangular membrane a	16 mm
Width of rectangular membrane b	14 mm
Average gap size between the walls c	3 mm
Thickness of rectangular membrane h	2 mm
Material parameter for silicone C_1	0.11
Material parameter for silicone C_2	0.02
Elastic coefficient of elastic rope k_c	0.02 N/mm
Compression elastic coefficient of lateral wall k_1	4×10^{-4} N/mm
Compression elastic coefficient of lateral wall k_2	$>1.3\times10^{-2}$ N/mm
Number of the air chambers n	7
Cross-sectional area of air tube S	7.08 mm^2
Fiber-layer-side length of ECPA l_b	87 mm
Force arm L_P	1 mm
Elastic coefficient of the Pneu-Nets actuator k_e	0.1 N/mm
Range of ECPA fingertip displacement x_0	45 mm

$$E=4C_2\left[1.3\left(v^2+\frac{1}{v^2}\right)+0.186\right]d^4h/u+2.84C_1\left(v+\frac{1}{v}\right)d^2h, \tag{2}$$

where d denotes the bulge height of the rectangular membrane, u and v respectively represent the area and the aspect ratio of the rectangular membrane, as shown in Figure 4(a), which can be given by

$$u=ab/4, \tag{3}$$

$$v=b/a. \tag{4}$$

To associate the relationship between the air pressure P and the deformation of the rectangular membrane, the energy method is used to analyze the expansion characteristics of the membrane, which can be expressed as

$$F_0\frac{d^2}{h}+\frac{1}{2}k_cd^2+E=P\Delta V+W, \tag{5}$$

where F_0 represents the pre-loading force, k_c represents the elastic coefficient of the elastic cord, W is the compression elastic potential energy of elastic rectangular membrane under the pre-loading force, ΔV denotes the volume enclosed by the undeformed membrane and the deformed membrane,

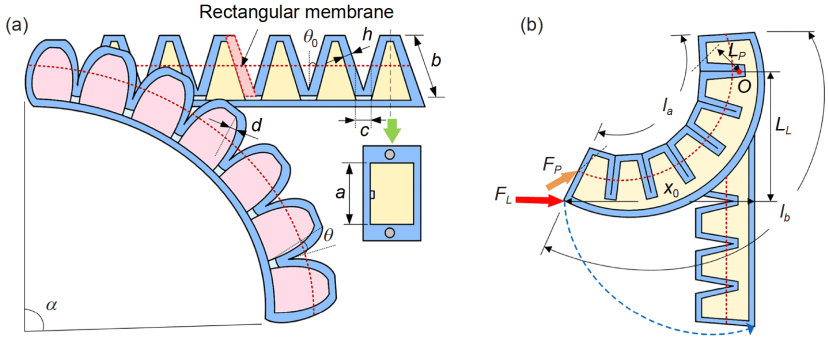

Figure 4 (Color online) Modeling and analysis of ECPA. (a) Geometry dimension of inflated and uninflated ECPA; (b) geometry dimension of the ECPA subjected to the horizontal external force.

which can be given by

$$\Delta V = 4ud\left[\int_0^1 (1-\tau^2)\mathrm{d}\tau\right]^2, \tag{6}$$

what is more, the compression elastic potential energy W can be given by

$$W = \frac{1}{2}k_1 d_1^{\ 2} + \frac{1}{2}k_2 d_2^{\ 2}, \tag{7}$$

where k_1 and d_1 represent the compression elastic coefficient and the average compression of the lateral wall when the air chambers of the ECPA are separated from each other, k_2 and d_2 denote the compression elastic coefficient and the average compression of the lateral wall when the air chambers of the ECPA are contact with each other.

According to eqs. (2)–(6), the relationship between the air pressure P and the bulge height of the rectangular membrane d is obtained by

$$\begin{aligned} P = {} & \frac{9}{4ab}\left[\frac{F_0}{h} + \frac{k_c}{2} + 2.84C_1 h\left(\frac{b}{a} + \frac{a}{b}\right)\right]d \\ & + \frac{hC_2}{a^2 b^2}\left[46.8\left(\frac{b^2}{a^2} + \frac{a^2}{b^2}\right) + 0.186\right]d^3 \\ & - \frac{9}{8abd}\left(k_1 d_1^{\ 2} + k_2 d_2^{\ 2}\right). \end{aligned} \tag{8}$$

The compression elastic potential energy of the lateral wall is relatively low, which can be ignored. According to the parameters of Table 1, eq. (8) can be written as

$$P = (0.5F_0 + 1.55) \times 10^{-2} d + 8.2 \times 10^{-4} d^3. \tag{9}$$

The bulge height of the lateral wall d is geometrically related to the theoretical bending angle of the actuator due to the expansion of a single lateral wall θ, which can be expressed by

$$d = \frac{b}{2\cos\theta}\left(\sin\theta + \frac{c}{b} + \sqrt{\frac{2c}{b}\sin\theta + \frac{c^2}{b^2}}\right), \tag{10}$$

where c is the average gap size between the walls of the air chambers in the initial state. The relationship between the actual single lateral bending angle $\Delta\theta$ and the expansion angle of the lateral wall θ can be given by

$$\Delta\theta = \theta - \theta_0, \tag{11}$$

where θ_0 is the initial angle between lateral walls of the adjacent air chambers, when the air chambers are contacted to each other under the pre-loading force, the initial angle θ_0 equals to 0°. Hence, the bending angle of the ECPA $\Delta\alpha$ can be obtained by

$$\Delta\alpha = 2(n-1)\Delta\theta, \tag{12}$$

where n represents the number of the air chambers.

The relationship of the pressure and the response speed of a single lateral wall is associated to analysis the response speed of ECPA. The Bernoulli's principle expresses the effect of air pressure on the deflation rate [31].

$$P = P_0 + \frac{1}{2}\rho v^2, \tag{13}$$

where P_0 is the atmospheric pressure, ρ represents the air density, v denotes the speed of air deflating. The ideal gas law can be written as

$$PV = nRT, \tag{14}$$

where V denotes the gas volume, R represents the ideal gas constant, T is the Kelvin thermodynamic temperature, and n is the number of moles, which can be expressed by

$$n = n_1 + \frac{Svt}{12V_m}, \tag{15}$$

where S is the cross-sectional area of the air tube, t is the deflation time, and V_m represents the molar volume of gas, n_1 is the number of moles enclosed by the undeformed membrane and the deformed membrane at 80 kPa. According to eqs. (13)–(15), we can get the relationship between the air pressure P and the deflation time t.

$$P = \frac{\left[n_1 - \frac{S\sqrt{2(P-P_0)}t}{V_m}\right]RT}{\Delta V}. \tag{16}$$

According to eq. (5), the air pressure P can also be written as

$$P = \frac{F_0 d^2}{h} + \frac{1}{2}k_c d^2 + E - W}{\Delta V}. \tag{17}$$

According to eq. (10)–(12), (16), and (17), we can associate the relationship between the pre-loading force F_0 and the response time t.

$$\begin{aligned} & \left(\frac{F_0}{h} + \frac{1}{2}k_c\right)\left\{\frac{b}{2\cos\left[\frac{\Delta\alpha}{2(n-1)} + \theta_0\right]}\left\{\sin\left[\frac{\Delta\alpha}{2(n-1)} + \theta_0\right] + \frac{c}{b} + \sqrt{\frac{2c}{b}\sin\left[\frac{\Delta\alpha}{2(n-1)} + \theta_0\right] + \frac{c^2}{b^2}}\right\}\right\}^2 + E - W \\ & \frac{}{RT} \\ & n_1 - \frac{}{} \\ & S\sqrt{2\left\{\left\{\left\{\left(\frac{F_0}{h} + \frac{1}{2}k_c\right)\left\{\frac{b}{2\cos\left[\frac{\Delta\alpha}{2(n-1)} + \theta_0\right]}\left\{\sin\left[\frac{\Delta\alpha}{2(n-1)} + \theta_0\right] + \frac{c}{b} + \sqrt{\frac{2c}{b}\sin\left[\frac{\Delta\alpha}{2(n-1)} + \theta_0\right] + \frac{c^2}{b^2}}\right\}\right\}^2 + E - W\right\}\frac{1}{\Delta V}\right\} - P_0\right\}t} \\ & \frac{}{V_m}. \end{aligned} \tag{18}$$

The stiffness of ECPA represents the capability of resisting deformation in response to external forces, which can be described by using a horizontal load that results in a displacement. To establish the relationship between external force and ECPA fingertip displacement, some assumptions are made to simplify the model. (1) When the fingertip is displaced at a constant speed, the side length of the ECPA changes uniformly. (2) When the ECPA is displaced by an external force, the trajectory of the fingertip is a circular arc. (3) Yield only occurs at the junction between the air chambers with the highest bending moment. (4) The pre-loading force offset by the deformation of ECPA itself in the initial state is evenly released with the displacement of the fingertip. (5) The fiber-layer-side length of the ECPA is assumed to be constant. (6) The air chambers contact each other after applying the pre-loading force. As shown in Figure 4(b), when the fingertip of the ECPA is subjected to the external force F_L, the force arm L_L of force F_L about point O is the largest, which means that the yield deformation is most likely to occur at point O. The moment balance about point O can be given by

$$F_L \cdot L_L = F_P \cdot L_P + M_A, \tag{19}$$

where F_P is the force generated by the elastic cord, L_P represents the force arm of F_P about point O, M_A denotes the drag torque of the Pneu-Nets actuator. And the force arm L_L of external force F_L about point O can be written as

$$L_L = \frac{l_b}{2}\left\{1+\sqrt{1-\left[\frac{l_b}{2(x_0-\Delta x)}\right]}\right\}, \tag{20}$$

where l_b denotes the fiber-layer-side length of ECPA, x_0 represents the range of ECPA fingertip displacement in the stiffness analysis, and the force generated by the elastic cord F_P can be obtained by

$$F_P = \frac{F_0}{x_0}\Delta x + k_c(l_b - l_a)\frac{\Delta x}{x_0}, \tag{21}$$

where l_a denotes the fiber-layer-side length of the ECPA. According to eq. (13)–(15), we can associate the relationship between the external force and ECPA fingertip displacement to analyze the stiffness of ECPA.

$$F_L\frac{l_b}{2}\left\{1+\sqrt{1-\left[\frac{l_b}{2(x_0-\Delta x)}\right]}\right\} = \frac{F_0}{x_0}\Delta x + L_P k_c(l_b - l_a)\frac{\Delta x}{x_0} + k_e \Delta x L_P, \tag{22}$$

where k_e presents the elastic coefficient of the Pneu-Nets actuator.

4 Experiment and results

4.1 Mechanical properties

The pre-tensioned elastic cord affects the stiffness of ECPA. A stiffness test is performed to validate the effect on the stiffness of the ECPA under different pre-loading forces (0, 1, 2, 3, 4, 5 N). The stiffness is described by using a load that results in a displacement of the ECPA under different pre-tending forces. As shown in Figure 5(b), the end of the ECPA and the force sensor (DYLY-105, China, scale 2 kg, accuracy 0.03%) are connected by the inelastic string. ECPA is fixed on the bracket, and the force sensor is fixed on the slide table which is driven by a motor to perform the motion at a constant speed. The force sensor moves slowly and uniformly (1 mm/s), driving the inelastic string to pull the end of the ECPA and deform it, ranging from 0 to 15 mm. The pulling force is measured by the force sensor. To improve the accuracy and credibility of the experimental results, all the groups of experiments are repeated three times to eliminate the random error.

What is more, the theoretical stiffness curves of ECPA can be calculated according to eq. (22). Figure 5(a) shows the experimental results (solid lines) and the theoretical predictions (broken curves) of the stiffness characterization of the

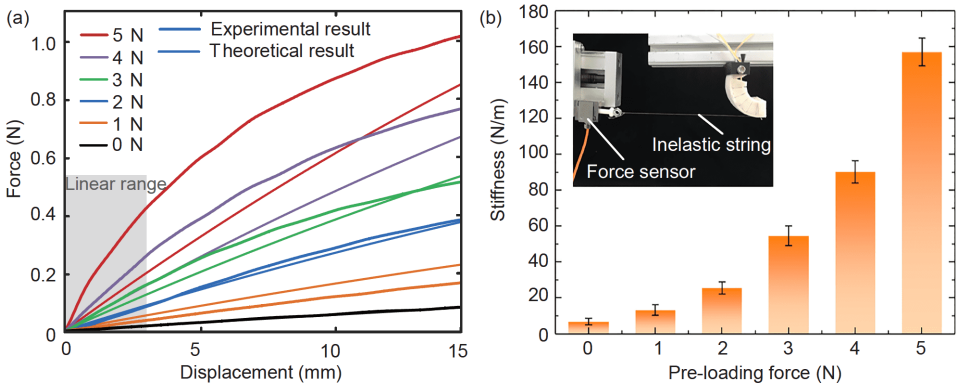

Figure 5 (Color online) Stiffness test. (a) Force-displacement curves of ECPA; (b) experimental setting and the stiffness under different pre-loading forces at the deflation range 0–3 mm.

ECPA under different pre-loading forces. The slope of the stiffness curve increases with the pre-loading force, which means that the pre-loading force of the elastic cord has a significant positive effect on improving the stiffness of the ECPA. Therefore, the stiffness of ECPA can be adjusted by simply changing the pre-loading force of the elastic cord.

As shown in Figure 5(a), the experimental force-displacement curves are almost linear at the deflation range 0–3 mm. To make the comparison more intuitive, linear fitting is conducted for the displacement interval 0–3 mm by the least square method, the slope of the fitting line is the stiffness value of ECPA. The comparison of the fitting stiffness under different pre-loading forces is shown in Figure 5(b). The value of stiffness increases significantly with the pre-loading force. The stiffness under 0 N pre-loading force is 6.87 N/m, and the stiffness arrives at 157 N/m when the pre-loading force is 5 N, thus, the stiffness of the finger is increased by at least 22 times. However, the air chamber connection of ECPA close to the fixed end is easy to yield due to the larger force arm, which is the area with weaker stiffness.

The ECPA needs to quickly evacuate the internal compressed gas, so that the actuator can achieve a rapid response. Due to the influence of inertia, when the ECPA is deflated and bent, the impact force is generated. An experiment is used to test the impact of ECPA when it returns to its natural state under different pre-loading forces (0, 1, 2, 3, 4, 5 N). As shown in Figure 6(a), the ECPA is fixed on the bracket. When the ECPA bends and stretches after being inflated, it is in a position far away from the sensor. Then the ECPA is deflated and quickly contracted, bending in the opposite direction and hitting the input end of the force sensor (DYLY-105, China, scale 2 kg, accuracy 0.03%) fixed on the bracket, then the impact force value is measured by the force sensor.

To reduce the random error, the experiment is repeated three times and the time-force curves are drawn with the average value, as shown in Figure 6(a). When the ECPA impacts the force sensor, the impact force of the end of the ECPA on the force sensor increases rapidly. After the impact force reaches its maximum value, it remains at a higher level for a short period of time, and then falls back to a lower stable value. In this process, the peak force recorded by the sensor is the maximum impact force produced by ECPA. What is more, the impact force generated by ECPA increases with the pretension force, and the duration of the impact is also positively related to the pre-loading force. The comparison of the peak impact force under different pre-loading forces is shown in Figure 6(b). The impact force without pre-loading force is 2.5 N, when the pre-loading force increases to 5 N, the impact force arrives at 6.5 N. The pre-loading force has a positive effect on increasing the impact force of PSPA.

ECPA can also reverse to bend during inflation to generate driving force. Therefore, the driving force generated by the inflated ECPA is also an important performance parameter. As shown in Figure 7, the ECPA and the force sensor are fixed on the bracket, the end of the finger in the initial state is in contact with the input end of the force sensor (DYLY-105, China, scale 2 kg, accuracy 0.03%). When the ECPA is inflated, the driving force is measured by the force sensor. In this experiment, the driving force of the ECPA under different pre-loading forces (0, 1, 2, 3, 4, 5 N) is tested. All the groups of experiments are repeated five times to eliminate the random error and improve the accuracy.

The experimental result is shown in Figure 7. The driving force of ECPA increases approximately linear with the air pressure, while the driving force is inversely related to the pre-loading force. Under the air pressure of 80 kPa, the driving force of ECPA with a 0 N pre-loading force is about 0.9 N, and the driving force of ECPA with a 5 N pre-loading force is about 4.5 N. Hence, ECPA has a large driving force when the pre-loading force is small. It is generally necessary to apply a small pre-tending force for improving the driving force of ECPA.

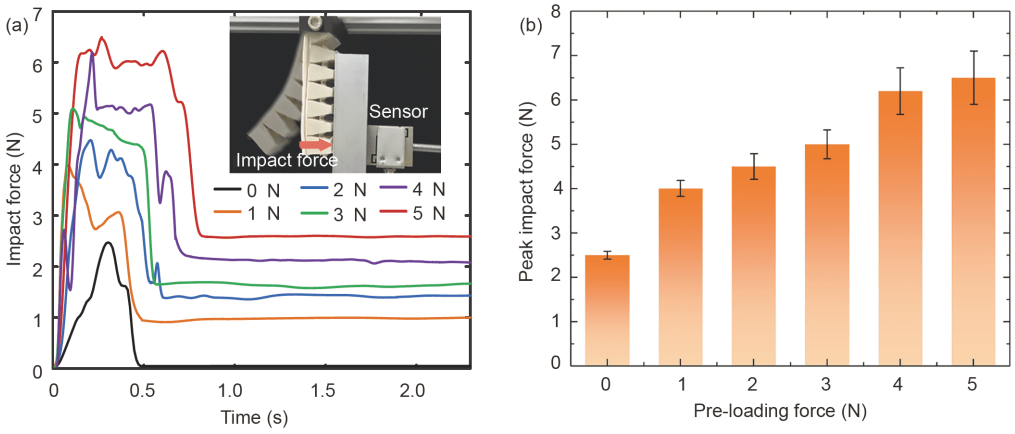

Figure 6 (Color online) Impact force test. (a) Experimental set-up and results of impact force test; (b) peak value of the impact force of the ECPA.

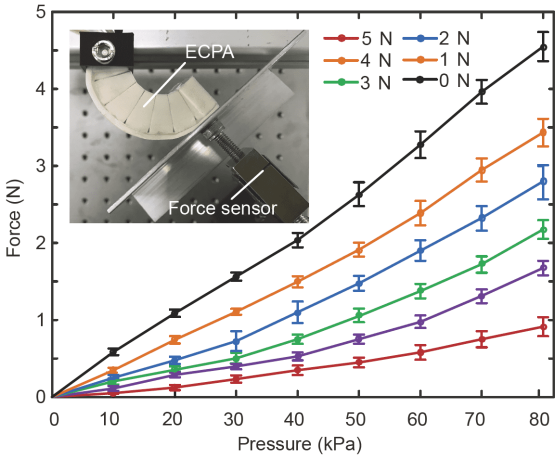

Figure 7 (Color online) Experimental setting and result of the driving force test.

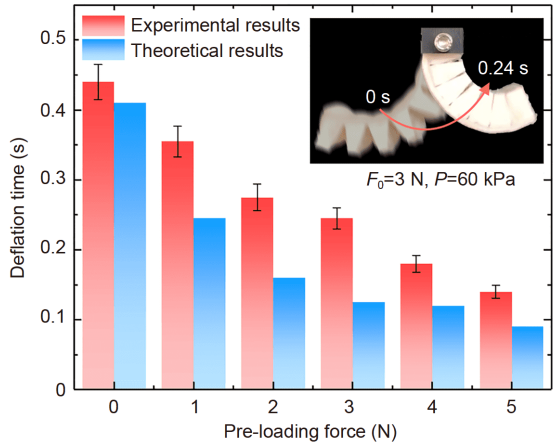

Figure 8 (Color online) The deflation response time of ECPA under different pre-loading forces.

4.2 Response characteristics

The deflation time of ECPA is the bending execution time, which is an important factor in determining response speed. High-speed camera is used to record the response of ECPA fixed on the bracket when evacuate under different pre-loading forces (0, 1, 2, 3, 4, 5 N), as shown in Figure 8. The actual deflation response time and theoretical deflation response time derived from eq. (18) of ECPA after filling with 80 kPa compressed gas are shown in Figure 8. The results indicate that the deflation response time of ECPA has a negative correlation with the pre-loading force. When the pre-loading force is 0 N, the actual deflation response time of ECPA is 0.44 s. However, as the pre-loading force is increased to 5 N, the deflation response time is reduced to 0.14 s. The response time is reduced by 68.2%. It can be concluded that the pre-loading force greatly speeds up the bending process which is the decisive process for the performance of pneumatic actuators.

The trajectories of the tip of ECPA (O') under different pressures (0, 1, 2, 3, 4 , 5 N) are shown in Figure 9(a). Different pre-loading forces cause different characteristics of the trajectory. A coordinate system is established with the fingertip of the natural state of ECPA without pre-loading force as the origin. With smaller pre-loading force, the trajectories are mainly located on the negative plane of the x-axis. However, with the large pre-loading force, the ECPA's trajectory curvature is smaller and closer to the fixed end of ECPA. Therefore, by adjusting the pre-loading force, the movement trajectories of different ranges and different curvatures of ECPA can be realized to adapt to more application scenarios.

The experimental and theoretical variation of bending angle of ECPA with air pressure and the relationship between the length and bending angle of ECPA are shown in Figure 9(b) and (c). The angle between the tangent of the ECPA tip and the vertical direction is defined as the bending angle of the finger α (the bending angle is positive in the clockwise direction and negative in the counterclockwise direction). As shown in Figure 9(b), the experimental results and the theoretical predictions calculated according to eq. (12) show that the pre-loading force affects the bending angle of ECPA. The experimental results show that when the pre-loading force is 0 N, the bending angle of ECPA varies from −150° to 50° under the air pressure of 0 to 80 kPa, and the bending angle of ECPA with 5 N pre-loading force changes from 0° to 200°. But the ECPA under different pre-loading forces has a same angle range ($\Delta\alpha$) of about 200°. As shown in Figure 9(c), due to the compression effect of the pretension force on the actuator, the length of the ECPA is shortened as the pretension force increases at the same bending angle.

As shown in Figure 9(d), the ratio of the air-chamber-side length to the fiber-layer-side length of the ECPA increases with the air pressure. Moreover, as the pre-loading force becomes larger, the curves of the length ratio become denser, indicating that as the pre-loading force increases, its increment of influence on the shape of ECPA decreases.

The volume change of the Pneu-Nets due to deformation of the elastomeric material defines the total amount of compressed gas that must be transported into it to achieve full bending; larger changes in volume require longer durations of pressurization to reach complete actuation [32]. To characterize the volume change required of fluid (in this experiment, water with low compressibility is used instead of gas) for the increase of internal pressure, an experiment is set to test the relationship of pressure and the volume of ECPA under different pre-loading forces (0, 1, 2, 3, 4 , 5 N). The experimental result is shown in Figure 10(a). It is indicated that the internal pressure of ECPA increases with the fluid volume, and the pre-loading force reduces the volume of fluid required to increase the internal pressure of the ECPA. As shown in Figure 10(b), under the action of 0 N pre-loading force, a volume change of 8 mL is required to achieve

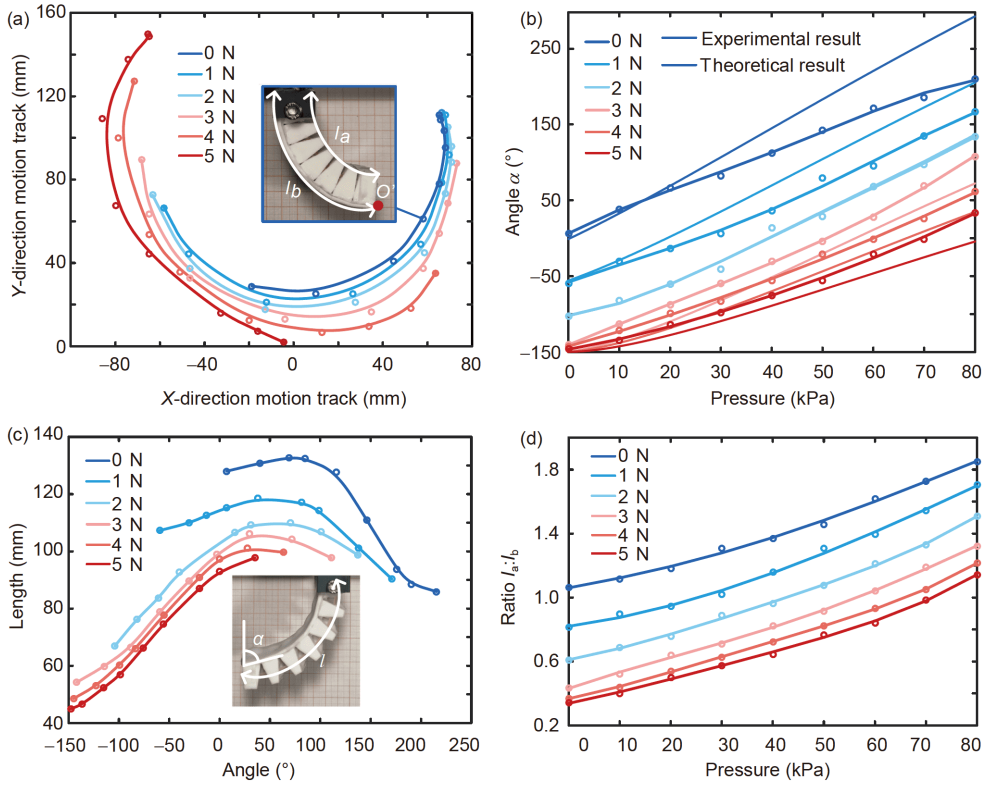

Figure 9 (Color online) Geometric response characteristics. (a) The trajectories of the ECPA tip under different pressures; (b) plot illustrating the bending angle of ECPA under different pre-loading forces varies with the air pressure; (d) the relationship between the length and bending angle of ECPA; (e) the graph depicting the ratio of the air chamber-side length to the fiber-layer-side length of the ECPA.

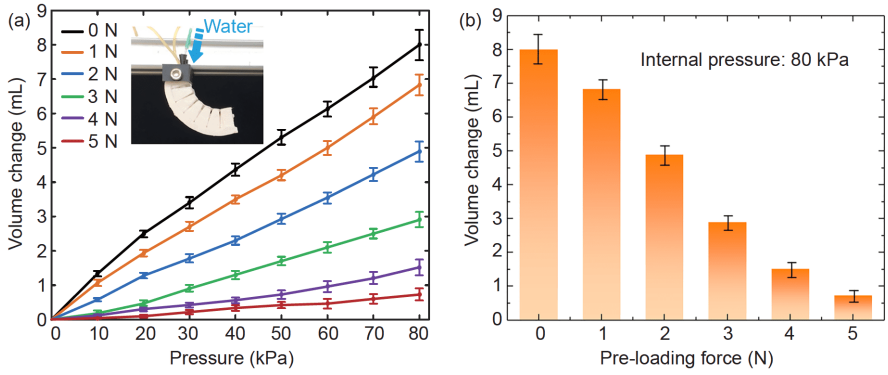

Figure 10 (Color online) The relationship of internal pressure and volume change of ECPA. (a) Experimental setting and result; (b) volume change required to reach internal pressure of 80 kPa.

an internal pressure of 80 kPa, while under the pre-loading force of 5 N, only 0.73 mL of volume change is required. The lower volume change caused by the pre-loading force reduces the time required for pressurization and deformation of ECPA.

5 Design and demonstration of fast-moving robots

5.1 The bionic quadruped running robot

Due to the fast response characteristics of ECPA, the elastic potential energy stored in ECPA can be released quickly after the internal gas is exhausted. Therefore, inspired by the quadruped, as shown in Figure 11(a), ECPA is suitable as the body part of a bionic quadruped running robot. As shown in Figure 11(b), the exoskeleton with two claws is fixed on each end of ECPA. The pre-tensioned elastic cord passes through the pneumatic actuator and the 3D-printed exoskeleton to constitute the bionic quadruped running robot. In order to improve the directional friction of the bionic quadruped running robot to prevent it from sliding backwards, small pieces of silicone are fixed on the front paw, and the friction

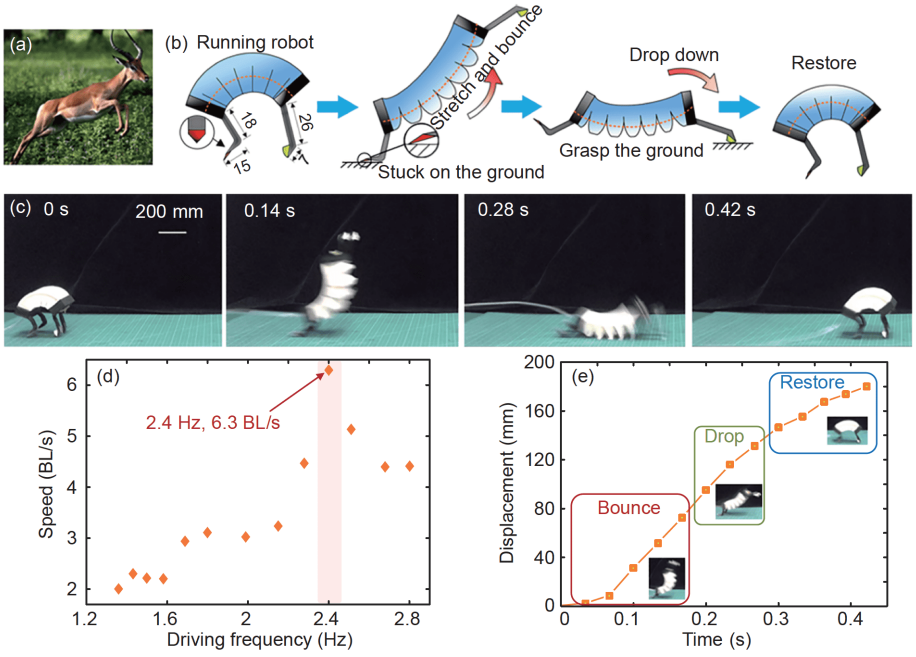

Figure 11 (Color online) The bionic quadruped running robot. (a) A running quadruped; (b) conceptual motion principle of running robot; (c) the actual movement process of the running robot (Movie S1); (d) the speed of bionic quadruped running robot under different driving frequencies; (e) the time-displacement curve of the bionic quadruped running robot under the driving frequency of 2.4 Hz.

sheets with sharp end are fixed on the hind paw. The prototype of the running robot is 68-mm long and 40-mm wide with a weight of 52 g. The elastic cord adjusts the response speed of ECPA, to reduce the response time and improve the locomotion speed of the running robot, the pre-loading force of the elastic cord is applied with a large pre-loading force (5 N). As shown in Figure 11(b) and (c), after inflating the ECPA, the bionic quadruped running robot is quickly drove to stretch. The sharp slices fixed on hind claws get stuck on the ground because of the high friction, the front claws are bounced, and then touch the ground under the action of its own gravity. When the gas inside ECPA is exhausted, the front claws grasp the ground through the silicone block and create a high friction. The hind claws move forward and the friction between sharp slices and the ground is reduced, and then quickly retract to complete one running cycle.

Wired power is used to amplify the periodic square wave signal (duty cycle 0.5) to drive the air pump and inflate the running robot. With the air pressure amplitude of 80 kPa, the speed of the running robot under different driving frequencies is shown in Figure 11(d). When the driving frequency of 2.4 Hz is applied, the speed of the running robot reaches its peak. Therefore, the bionic quadruped running robot achieves a running speed of 6.3 body length/s (428 mm/s) when pressurized at 80 kPa at an actuation frequency of 2.4 Hz, the time-displacement curve during running is shown in Figure 11(e). In the process of running, the dropping process takes a short time, while the process of bouncing and restoring is relatively long.

As shown in Table 2 [19–21,27,33,34], the speed of the bionic quadruped running robot is compared with that of the running soft robots. These running soft robots demonstrate a relatively slow speed in the range of 0.01 to 2.68 BL/s because of the low response speed or output force. Due to the elastic energy stored in EPCA, the bionic quadruped running robot is provided with fast response and high stiffness to adapt to higher driving frequency and overcome the resistance to move at least twice as fast as other running robots, outperforming most of the reported soft running robots [27]. Therefore, the EPCA-based quadruped running robot is called a fast-moving robot.

5.2 The bionic manta ray swimming robot

Then, inspired by the manta ray, the ECPA can also serve as the body part of an underwater swimming robot. As shown in Figure 12(a), the exoskeleton of the bionic manta ray swimming robot consists of silicone thin film and 3D-printed L-shaped frame which is covered by the silicone film. The pre-tensioned elastic cord passes through the pneumatic actuator and fixes the exoskeleton on each end of ECPA to constitute the bionic manta ray swimming robot. The prototype of the bionic manta ray swimming robot is 95-mm long and 145-mm wide with a weight of 65 g. As shown in Figure 12(b), the swimming robot achieves a flapping action like manta ray in the water. To reduce the response time of ECPA and improve the locomotion speed of the bionic manta ray swimming robot, the pre-loading force of the elastic cord

is set as 5 N. As shown in Figure 12(c), the ECPA alternates between inflation and deflation, resulting in the repeated bending deformation of the actuator, driving the fins fixed on the ECPA to flap up and down. As the air pressure inside the ECPA changes periodically, the fins are flapping to actuate the robot to swim forward. Figure 12(d) shows the comparison of swimming speed between different driving frequencies. When the driving frequency is 1.4 Hz, the bionic manta ray swimming robot reaches the maximum speed of 1.07 body length/s (102 mm/s) with pressurized at 80 kPa. The time-displacement curve under the driving frequency of 1.4 Hz is shown in Figure 12(e), during the swimming process, the contributions of upward flapping and the downward flapping to the swimming displacement are basically the same.

As shown in Table 3 [27,35–39], the speed of the bionic manta ray swimming robot is compared with that of other types of swimming soft robots which utilize different driving methods. Because of the large output force generated by pneumatic driving method, the resistance of water has less

Table 2 Comparison of running velocity between the proposed running robot and various reported locomotive soft robots

Refs.	Actuator type	Robot type	Body length (mm)	Maximum speed (BL/s)
Duduta et al. [20]	Dielectric elastomer	4 legs robot	20	1
Li et al. [19]	Dielectric elastomer	Rolling robot	49.66	0.95
Mao et al. [33]	Shape memory alloy	Starfish-like robot	228	0.01
Du et al. [34]	Shape memory alloy	Rolling robot	145	0.18
Liao et al. [21]	Pneumatic	Snake robot	160	0.19
Tang et al. [27]	Pneumatic	Spine-inspired robot	70	2.68
This work	Pneumatic	Quadruped robot	68	6.3

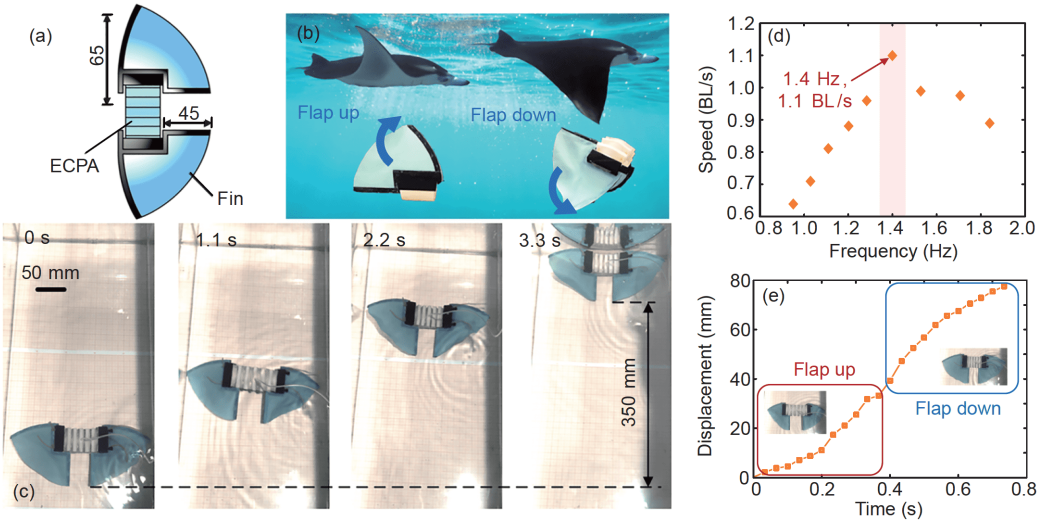

Figure 12 (Color online) The bionic manta ray swimming robot. (a) The prototype of the bionic manta ray swimming robot; (b) side view of the swimming state of the bionic manta ray swimming robot compared with the manta ray; (c) the actual movement process of the bionic manta ray swimming robot (Movie S2); (d) the speed of bionic manta ray swimming robot under different driving frequencies; (e) the time-displacement curve of the bionic manta ray swimming robot under the driving frequency of 1.4 Hz.

Table 3 Comparison of swimming velocity between the proposed swimming robot and various reported underwater soft swimmers

Refs.	Actuator type	Robot type	Body length (mm)	Maximum speed (BL/s)
Shintake et al. [35]	Dielectric elastomer	Fish robot	148	0.25
Bartlett et al. [36]	Shape memory alloy	Fish robot	20	0.15
Cianchetti et al. [37]	Shape memory alloy	Octopus robot	167	0.3
Suzumori et al. [38]	Pneumatic	Manta swimming robot	150	0.67
Fan et al. [39]	Pneumatic	Frog robot	175	0.43
Tang et al. [27]	Pneumatic	Sheet-based fin robot	150	0.78
This work	Pneumatic	Manta ray robot	95	1.07

effect on pneumatic swimming robots. Therefore, the pneumatic swimming robots have the faster moving speed, demonstrating the speed in the range of 0.43 to 0.78 BL/s. Furthermore, due to the fast response characteristics and high rigidity, the bionic manta ray swimming robot reaches the movement speed of 1.07 BL/s, outperforming most of the reported soft swimming robots [27]. Therefore, the EPCA-based bionic manta ray swimming robot is also called a fast-moving robot.

However, due to the friction generated by the hind legs and the stretch of the Pneu-Nuts actuator, the bionic quadruped running robot generates extra bouncing movement, transforming part of the kinetic energy into gravitational potential energy, reducing the speed of movement. What is more, the wide fin of bionic manta ray swimming robot provides enough propulsion but also generates great resistance, causing a significant vertical movement of the locomotion robot and consume the power generated by ECPA. Nevertheless, these locomotion robots still achieve fast movement speeds, indicating that the locomotion robots based on ECPA have great potential for improvement. What is more, as shown in the experimental results, the speed of the moving robots based on ECPA can be adjusted by changing the frequency of inflation.

6 Discussion and conclusion

In this work, we present a simple design strategy for pre-tensioned actuator, exploiting the significantly improved elastic energy storage to enhance the capability of the actuator. The all-flexible actuator shows rapid response speed and high performance due to the pre-loading force of the elastic cord. To research the effect of pre-loading force on the performance of ECPA, the modeling of ECPA is established, what is more, the mechanical properties and morphological characteristics of ECPA are tested. Experimental results and theoretical predictions both indicate that the pre-loading force improves the stiffness and the response speed of ECPA. Experimental results show that the deflation response speed of ECPA is increased by at least 3.1 times with the action of elastic component, as the pre-tightening force of the elastic cord increases, the deflation speed of ECPA also increases. What is more, the stiffness of ECPA is increased by 22 times, similarly, the stiffness of ECPA is also proportional to the pre-loading force of the elastic cord. In addition, mechanical characteristics including the impact force generated during deflation and the output force during inflation can also be regulated by the pre-loading force. Moreover, the difference in pre-loading force also affects the morphological characteristics of ECPA such as the bending angle and the end trajectory. The pre-loading force of the elastic cord is able to adjust and improve the performance of ECPA in many aspects. Hence, based on the ECPA, the bionic quadruped running robot and the bionic manta ray swimming robot can reach the fast locomotion speed. The fast response characteristics and high strength of ECPA enable running and swimming robots to adapt to faster driving frequencies and overcome the resistance. The bionic quadruped running robot runs at an average locomotion speed of 6.3 BL/s and the bionic manta ray swimming robot achieves an average speed of 1.1 BL/s.

The ECPA provides a new solution for improving the mechanical properties and the response speed of pneumatic actuator. Experimental results show that the ECPA, which remains fully flexible, achieves a wide range of bi-directional bending and a very fast response speed. In addition, the mechanical properties of ECPA, such as stiffness and output force, have been improved and the mechanical properties can be adjusted by changing the pre-loading force. Nevertheless, the weak part of ECPA with lower stiffness makes it susceptible to yielding, and the pre-loading force negatively affects the output force. In addition, it is difficult to achieve precise control of ECPA. In our future work, the design of the ECPA will be improved to strengthen the rigidity, avoiding yielding of the end of ECPA. More importantly, the response speed of ECPA will be further accelerated, and the adverse effects of the pre-loading force on ECPA will be reduced. Meanwhile, we will further optimize the structure and control of the running robot and swimming robot to achieve more rapid and efficient movements and we will further explore the factors that affect the movement speed of the robots.

This work was supported by the National Natural Science Foundation of China (Grant Nos. 91748118 and 12032015), the Program of Shanghai Key Laboratory of Spacecraft Mechanism, the National Natural Science Foundation for Distinguished Young Scholars of China (Grant No. 11625208), the Program of Shanghai Academic/Technology Research Leader (Grant No. 19XD1421600), and the National Postdoctoral Program for Innovative Talents (Grant No. BX20190201).

Supporting Information

The supporting information is available online at tech.scichina.com and link.springer.com. The supporting materials are published as submitted, without typesetting or editing. The responsibility for scientific accuracy and content remains entirely with the authors.

1 Rus D, Tolley M T. Design, fabrication and control of soft robots. Nature, 2015, 521: 467–475
2 Tang L, Zhu L M, Zhu X Y, et al. Confined spaces path following for cable-driven snake robots with prediction lookup and interpolation algorithms. Sci China Tech Sci, 2020, 63: 255–264
3 Wang Y Z, Gupta U, Parulekar N, et al. A soft gripper of fast speed and low energy consumption. Sci China Tech Sci, 2019, 62: 31–38
4 Nemiroski A, Shevchenko Y Y, Stokes A A, et al. Arthrobots. Soft Robotics, 2017, 4: 183–190
5 Qin L, Liang X, Huang H, et al. A versatile soft crawling robot with rapid locomotion. Soft Robotics, 2019, 6: 455–467
6 Wang W, Ahn S H. Shape memory alloy-based soft gripper with

variable stiffness for compliant and effective grasping. Soft Robotics, 2017, 4: 379–389
7 Yang Y, Chen Y, Li Y, et al. Bioinspired robotic fingers based on pneumatic actuator and 3D printing of smart material. Soft Robotics, 2017, 4: 147–162
8 Yang Y, Chen Y, Li Y, et al. Novel variable-stiffness robotic fingers with built-in position feedback. Soft Robotics, 2017, 4: 338–352
9 Al Abeach L A T, Nefti-Meziani S, Davis S. Design of a variable stiffness soft dexterous gripper. Soft Robotics, 2017, 4: 274–284
10 Sun T, Chen Y, Han T, et al. A soft gripper with variable stiffness inspired by pangolin scales, toothed pneumatic actuator and autonomous controller. Robotics Comput-Integrat Manufact, 2020, 61: 101848
11 Wei Y, Chen Y, Ren T, et al. A novel, variable stiffness robotic gripper based on integrated soft actuating and particle jamming. Soft Robotics, 2016, 3: 134–143
12 Yang D, Verma M S, Lossner E, et al. Negative-pressure soft linear actuator with a mechanical advantage. Adv Mater Technol, 2017, 2: 1600164
13 Yoshida S, Morimoto Y, Zheng L, et al. Multipoint bending and shape retention of a pneumatic bending actuator by a variable stiffness endoskeleton. Soft Robotics, 2018, 5: 718–725
14 Guo X Y, Li W B, Gao Q H, et al. Self-locking mechanism for variable stiffness rigid-soft gripper. Smart Mater Struct, 2020, 29: 035033
15 Jiang Y K, Chen D S, Liu C, et al. Chain-like granular jamming: A novel stiffness-programmable mechanism for soft robotics. Soft Rob, 2019, 6: 118–132
16 Sun Y, Yap H K, Liang X, et al. Stiffness customization and patterning for property modulation of silicone-based soft pneumatic actuators. Soft Robotics, 2017, 4: 251–260
17 Scarfogliero U, Stefanini C, Dario P. The use of compliant joints and elastic energy storage in bio-inspired legged robots. Mechanism Machine Theor, 2009, 44: 580–590
18 Anderson I A, Gisby T A, McKay T G, et al. Multi-functional dielectric elastomer artificial muscles for soft and smart machines. J Appl Phys, 2012, 112: 041101
19 Li W B, Zhang W M, Zou H X, et al. A fast rolling soft robot driven by dielectric elastomer. IEEE/ASME Trans Mechatron, 2018, 23: 1630–1640
20 Duduta M, Clarke D R, Wood R J. A high speed soft robot based on dielectric elastomer actuators. In: Proceedings of the 2017 IEEE International Conference on Robotics and Automation (ICRA). Singapore, 2017. 4346–4351
21 Liao B, Zang H, Chen M, et al. Soft rod-climbing robot inspired by winding locomotion of snake. Soft Robotics, 2020, 7: 500–511
22 Yang C, Kang R, Branson D T, et al. Kinematics and statics of eccentric soft bending actuators with external payloads. Mechanism Machine Theor, 2019, 139: 526–541
23 Satheeshbabu S, Krishnan G. Modeling the bending behavior of fiber-reinforced pneumatic actuators using a pseudo-rigid-body model. J Mech Robotics, 2019, 11: 3
24 Li Y, Chen Y, Ren T, et al. Precharged pneumatic soft actuators and their applications to untethered soft robots. Soft Robotics, 2018, 5: 567–575
25 Wang Z, Torigoe Y, Hirai S. A prestressed soft gripper: Design, modeling, fabrication, and tests for food handling. IEEE Robot Autom Lett, 2017, 2: 1909–1916
26 Pal A, Goswami D, Martinez R V. Elastic energy storage enables rapid and programmable actuation in soft machines. Adv Funct Mater, 2019, 30: 1906603
27 Tang Y, Chi Y, Sun J, et al. Leveraging elastic instabilities for amplified performance: Spine-inspired high-speed and high-force soft robots. Sci Adv, 2020, 6: eaaz6912
28 Hao Y, Wang T, Ren Z, et al. Modeling and experiments of a soft robotic gripper in amphibious environments. Int J Adv Robotic Syst, 2017, 14: 172988141770714
29 Polygerinos P, Lyne S, Wang Z, et al. Towards a soft pneumatic glove for hand rehabilitation. In: Proceedings of the 2013 IEEE/RSJ International Conference on Intelligent Robots and Systems. Tokyo, 2011. 1512–1517
30 Wang J, Fei Y, Pang W. Design, modeling, and testing of a soft pneumatic glove with segmented PneuNets bending actuators. IEEE/ASME Trans Mechatron, 2019, 24: 990–1001
31 Fei Y Q, Pang W. Analysis on nonlinear turning motion of multi-spherical soft robots. Nonlinear Dyn, 2016, 88: 883–892
32 Mosadegh B, Polygerinos P, Keplinger C, et al. Pneumatic networks for soft robotics that actuate rapidly. Adv Funct Mater, 2014, 24: 2163–2170
33 Mao S, Dong E, Jin H, et al. Gait study and pattern generation of a starfish-like soft robot with flexible rays actuated by SMAs. J Bionic Eng, 2014, 11: 400–411
34 Du Y, Xu M, Dong E B, et al. A novel soft robot with three locomotion modes. In: Proceedings of the 2011 IEEE International Conference on Robotics and Biomimetics. Phuket, 2011. 98–103
35 Shintake J, Cacucciolo V, Shea H, et al. Soft biomimetic fish robot made of dielectric elastomer actuators. Soft Robotics, 2018, 5: 466–474
36 Bartlett M D, Kazem N, Powell-Palm M J, et al. High thermal conductivity in soft elastomers with elongated liquid metal inclusions. Proc Natl Acad Sci USA, 2017, 114: 2143–2148
37 Cianchetti M, Calisti M, Margheri L, et al. Bioinspired locomotion and grasping in water: The soft eight-arm octopus robot. Bioinspir Biomim, 2015, 10: 035003
38 Suzumori K, Endo S, Kanda T, et al. A bending pneumatic rubber actuator realizing soft-bodied manta swimming robot. In: Proceedings of the 2007 IEEE International Conference on Robotics and Automation (ICRA). Rome, 2007. 4975–4980
39 Fan J, Wang S, Yu Q, et al. Swimming performance of the frog-inspired soft robot. Soft Robotics, 2020, 7: 615–626